Catalysis Science & Technology

Accepted Manuscript

ROYAL SOCIETY OF CHEMISTRY

www.rsc.org/catalysis

Carbon Nitride Nanosheet/Metal-Organic Framework Nanocomposites with Synergistic Photocatalytic Activities

Jindui Hong,[a] Chunping Chen,[b] Franky E. Bedoya,[a] Geoff H. Kelsall,[a] Dermot O'Hare,[b] and Camille Petit*[a]

[a]*Department of Chemical Engineering, Imperial College London, South Kensington Campus, London SW7 2AZ, UK*

[b]*Chemistry Research Laboratory, Department of Chemistry, University of Oxford, 12 Mansfield Road, Oxford, OX1 3TA, UK*

[*] *E-mail: camille.petit@imperial.ac.uk; Phone: +44 (0)20 7594 3182 (Petit C.)*

Abstract

Heterogeneous photocatalysis plays a key role in the implementation of novel sustainable technologies, e.g. CO_2 conversion into fuel, H_2 production from water or organics degradation. The progress of photocatalysis relies on the development of tuneable photocatalysts and particularly the ability to build nanocomposites exhibiting synergistic properties with reduced electron-hole recombination rates. We report for the first time the *in situ* synthesis of nanocomposites of carbon nitride nanosheets (CNNSs) and metal-organic frameworks (MOFs) for application as photocatalysts. This approach leads to the 'nano-scale mixing' of the components, thereby enabling a greater performance compared to other types of 2D materials/MOF composites typically obtained via physical mixing. The objective is to take advantage of the complementary features of the materials while forming a heterojunction. The structural, chemical, photophysical and electrochemical properties of the nanocomposites are characterized and compared to those of the parent materials and

their physical mixture. The nanocomposites retain the high specific surface area and strong visible light absorbance of MIL-100(Fe). The intimate contact between the CNNSs and the MOF particles is found to promote the electron-hole separation significantly due to the formation of a heterojunction. Hence, more efficient photocatalytic dye degradation is achieved over the composites than the physical mixture.

1 Introduction

Photocatalysis, and particularly heterogeneous photocatalysis, is recognized to have a key role in paving the way towards sustainability. Solar light can indeed be harvested to drive reactions of relevance to the energy and environmental sectors. Specific examples include the conversion of CO_2 into fuel, the production of H_2 from water or the degradation of organic contaminants.[1-4] Heterogeneous photocatalysis relies on the development of photocatalysts that combine high-efficiency, low-cost, long-term stability and are environmentally benign. Since the discovery of TiO_2 photocatalyst,[5] a library of other materials including heterogeneous metal oxides, metal sulfides, oxynitrides and oxysulfides have been investigated for photocatalytic applications.[1,6] More recently, the field has been extended to include finely tuned photocatalysts in the form of nanocomposites, which can exhibit synergistic properties while opening the route for: (i) high surface area, hence enhanced reactant/catalysts interactions via adsorption, (ii) inhibited electron-hole recombination rates, (iii) uniform dispersion of photocatalytically active sites and (iv) broadening of the usable light spectrum. These efforts are all directed towards the common goal of addressing the limitations of 'conventional' photocatalysts in terms of efficiency, cost, robustness and sustainability.

Carbon nitride (CN), a recently developed crystalline polymeric photocatalyst[7-10] contains earth-abundant elements of carbon and nitrogen and can be easily synthesized via the calcination of low-cost organic precursors like urea. It is highly stable in a wide range of pH (0-14), upon heating (up to

550 ºC) and under photo-irradiation. CN, the band gap of which is typically ca. 2.7 eV,[7] has been used to catalyse a number of reactions and particularly: water splitting,[7,10] carbon dioxide reduction[11-13] and degradation of contaminants in water.[14,15] Its purely organic nature and facile synthesis represent the key strengths of the material. However, CN exhibits a relatively low surface area of 10 - 70 $m^2 g^{-1}$, depending on the synthesis method. A higher porosity and surface area would enable greater adsorption densities of the reactants and thereby favour photocatalytic reactions.

On the other hand, metal-organic frameworks (MOFs) are highly porous crystalline materials formed through the coordination of metallic ions and organic ligands. Due to their porous structure and easily tuneable properties, they have been applied in gas storage/separation,[16] catalysis,[17,18] chemical sensing[19] and drug delivery,[20] etc. More recently, research has focused on the photocatalytic properties of MOFs.[4,21] Unlike many other photocatalysts, MOFs benefit from a high surface area, a controllable pore size and tuneable light harvesting capacity.[4] To date, several MOFs including MOF-5,[22] MOF-253-Pt,[23] UiO-66,[24-26] UiO-67,[27] NTU-9,[28] MIL-53(Fe),[29,30] MIL-88(A)(Fe),[31] MIL-88B(Fe),[30,32] MIL-100(Fe),[32-34] MIL-101(Fe)[30,33,35] and MIL-125(Ti),[36,37] etc. have been studied as photocatalysts for water splitting, CO_2 conversion, organic transformation and contaminants degradation. Like all single-component photocatalysts, MOFs, after light excitation, is subject to electron-hole recombination at significant rates. Formation of heterojunction nanocomposites has proved an effective way to address this issue, thereby increasing photocatalytic activity.[38-40] Nevertheless, hitherto only few studies on MOFs-based heterojunction photocatalysts have been reported.[25,26,34,35,37] For example, UiO-66/CN was fabricated using a thermal annealing process and exhibited enhanced photocatalytic H_2 production from aqueous solutions due to the heterojunction formed.[26] In another example, CN/MIL-125(Ti) was reported to enhance the photocatalytic degradation of dyes in aqueous solutions.[37]

Herein, we report the *in situ* synthesis of CNNSs-MOF nanocomposites for application as photocatalysts. The objective of this work was to take advantage of the complementary features of MOFs and CN while inhibiting electron-hole recombination rates and therefore address weaknesses observed in the past with other MOF-based photocatalysts. MIL-100(Fe), a porous iron(III) carboxylate, was selected as the representative MOF as it is relatively inexpensive,[41] non-toxic,[41] water-/photo-stable[42] and visible light responsive.[35] In fact, MIL-100(Fe) has already been used for the photocatalytic oxidation of benzyl alcohol,[41] reduction of Cr(VI)[43] and photocatalytic degradation of Rhodamine 6G,[33] methylene blue,[34] and methyl orange.[43] Unlike most recent studies focusing on CN/MOF,[26,44] the nanocomposites developed as described below were not obtained via physical mixing. Instead, CN was first exfoliated to form two-dimensional (2D) carbon nitride nanosheets (CNNSs) with graphene-like structure, which have better electron mobility and more surface active sites compared to the bulk material.[15,45,46] Therefore, these nanosheets could be used as 'building blocks' for the formation of the nanocomposites and allowed for a homogeneous distribution of CNNSs at the nanoscale. The MOF crystals were then grown *in-situ* in the presence of the CNNSs. This approach is similar to that adopted earlier to build MOF/graphene oxide composites as materials for gas adsorption.[41,47-50] Although many semiconductor/MOF nanocomposites have been reported so far, most of the adopted semiconductors are in the form of bulk structure or nanoparticles and 2D semiconductor/MOF nanocomposites are still very rare up to date. Most often the 'mixing' of the two components is at the macroscale while a 'nano-scale mixing' would offer greater electron transfer. For instance, we noticed the very recent study by Shi et al. in which a CNNSs/UiO-66 composite was produced and used for CO_2 reduction.[51] The carbon nitride nanosheet and MOF were synthesized separately like other similar composites. While promising results were reported, we suspect thata more 'intimate' contact between the MOF crystals and the CNNSs would lead to even greater performance. To the best of our knowledge, our work on CNNSs/MIL-100(Fe), presented below, is the first example of *in-situ* synthesis of 2D semiconductor/MOF nanocomposite photocatalyst. The

nanocomposites obtained were characterized systematically and tested for the photocatalytic degradation of RhB to evaluate the effect of the heterojunction structure.

2 Experimental

2.1 Material synthesis

2.1.1 Synthesis of carbon nitride and carbon nitride nanosheets

To synthesize carbon nitride (CN), urea (20 g, molecular biology grade, Sigma-Aldrich) was placed in a crucible, covered with a lid and heated at 550 °C for 4 h with a ramping rate of 5 °C min^{-1} using a muffle furnace (Carbolite CWF 1200 chamber). About 1 g of yellow powder was collected.

The CN nanosheets, referred to as CNNSs, were prepared via liquid exfoliation. Briefly, CN powder (80 mg) was dispersed in ethanol (40 mL) and then exfoliated for 60 min using a probe sonicator (CL-334, Qsonica, 500 W, 90% amplitude). The resulting suspension was separated via centrifugation at 6,000 rpm for 5 min and the supernatant was collected. The CNNSs were obtained by centrifuging the supernatant at 15, 000 rpm for 15 min to remove the ethanol and then dried in a 60 °C oven.

2.1.2 Synthesis of MIL-100(Fe)

MIL-100(Fe) was synthesized using a modified non-hydrothermal method:[51] Iron(III) chloride hexahydrate ($FeCl_3 \cdot 6H_2O$, ACS reagent, 97%, Sigma-Aldrich, 20 mmol, 5.40 g) and benzene-1,3,5-tricarboxylic acid (H_3BTC, 95%, Sigma-Aldrich, 18 mmol, 3.78 g) were mixed in deionized water (12 mL) in a 100 mL bottle with a cap. The mixture was heated at 95 ºC for 18 h without stirring. The product obtained was washed with ethanol/H_2O (v/v=1/1) and centrifuged at 6,000 rpm for 5 min until the supernatant was clear. The wet sample was dried firstly at 60 °C under ambient pressure and then at 120 ºC under vacuum overnight. About 1.20 g of sample was obtained after drying. 'MIL' is used to denote the sample obtained.

2.1.3 Synthesis of CNNSs-MIL-100(Fe) nanocomposites

The synthesis of the nanocomposites followed a similar approach to that of MIL. After mixing the MIL precursors, a specific amount of CNNSs (6, 12, 24, 60 mg for 0.5, 1, 2 and 5 wt% CNNSs in CNNSs-MIL, respectively) in deionized water (12 mL) was added to the MIL precursor mixture. The same heat treatment, washing and drying procedures to those of MIL were then applied. The samples obtained are referred to as CNNSs-MIL-X wt%, where 'X wt%' represents the weight percent of CNNSs in the sample.

2.2 Materials characterisation

Structural and textural properties: The powder X-ray diffraction (XRD) patterns were obtained from a XRD diffractometer (PANalytical X'Pert PRO) in reflection mode at 40 kV and 40 mA using Cu Kα radiation (α1 = 1.54057 Å, α2 = 1.54433 Å, weighted average = 1.54178 Å). Nitrogen sorption analysis was performed using a porosity analyser (Micromeritics, 3Flex) at -196 ºC. Prior to the analysis, samples were dried overnight at 120 ˚C under low vacuum and then further degassed overnight at 120 ºC (around 0.2 mbar). Finally, the samples were in-situ degassed on the sorption analyzer at 120 ºC for 4 h (around 0.0030 mbar). The surface areas were calculated using the Brunauer-Emmett-Teller method.[52] The total volume of pore was determined from the volume of N_2 adsorbed at $P/P_0 = 0.97$. The micropore volume was calculated using the t-plot method.[53] The morphology of samples was observed by using a JEOL 2100 Transmission Electron Microscopy (TEM). The thickness of CNNSs was measured over an Agilent 5400 atomic force microscope (AFM) using tapping mode. The data was processed using a WSxM software.[54]

Chemical and thermal properties: Fourier Transform-Infrared (FT-IR) spectra in the range of 600-4000 cm^{-1} were recorded using a Perkin-Elmer Spectrum 100 Spectrometer equipped with an attenuated total reflectance (ATR) accessory. Thermogravimetric analysis (TGA) was carried out in the temperature range from 25 °C to 900 °C in air (100 mL min^{-1}) using a thermogravimetric analyser (NETZSCH TG 209 F1).

Photophysical and electrochemical properties: The UV–vis diffuse reflectance spectra (UV-vis DRS) within 250-800 nm were obtained on a UV–vis spectrometer (Perkin-Elmer Lambda 35) equipped with a Labsphere RSA-PE-20 diffuse reflectance accessory. Samples (20 mg) were diluted 100 times in $BaSO_4$ (ReagentPlus®, 99%, Sigma-Aldrich) and then placed in a quartz cuvette for the measurement. $BaSO_4$ was used as a standard reference and the recorded reflectance was converted using the Kubelka-Munk equation.[55] Photoluminescence (PL) emission spectra were recorded on a Perkin-Elmer LS55 luminescence spectrometer across 400 to 750 nm at room temperature with an excitation wavelength of 395 nm for MIL-based samples. The excitation and emission slit width were set both at 5 nm and scanning rate set at 500 $nm \cdot min^{-1}$. Samples were prepared in deionized water at a concentration of 0.2 mg mL^{-1} and analysed using a 1 cm path length quartz cell. Electrochemical impedance spectroscopy (EIS) measurements were carried out to determine the band edge/ potentials of MIL and CNNSs using the Mott-Schottky approach.

EIS measurements were made in a potentiostat/galvanostat Autolab PGSTAT 100 electrochemical station and a three-electrode cell: the sample-deposited fluorine-doped tin oxide (FTO, TEC-8, ~8 Ω/sq, 3 mm) slide as the working electrode, 2 cm^2 Pt sheet as the counter electrode and AgCl/Ag (saturated KCl) as the reference electrode. The aqueous electrolyte was Na_2SO_4 solution (0.2 M) de-oxygenated by bubbling with N_2 for 30 min. For electrode preparation, the FTO slide was cleaned with acetone and de-ionized water and then dried in 60 ºC oven. The conductive side of the FTO substrate was then covered fully with epoxy resin except for a 1 × 1 cm^2 of working area in one end and another 1 × 1 cm^2 for the electrical connection. The sample slurry (10 mg sample in 1 mL ethanol) was dropped on the working area of the FTO slide and dried at 60 ºC in an oven.

2.3 Photocatalytic evaluation

Dye degradation was selected as a way to test the photocatalytic performance of the nanocomposites. In a typical experiment, 10 mg of sample was dispersed in 50 mL of Rhodamine B (RhB, Dye content

97 %, Sigma-Aldrich) aqueous solution (50 mg L^{-1}). The suspension was stirred in the dark for 2 h to reach the adsorption equilibrium prior to photocatalytic reaction. Hydrogen peroxide (H_2O_2, 30 wt%, Sigma-Aldrich) was added to the suspension (0.01 M, 50 mL) before turning on the light. A 150 W xenon arc lamp (LOT-Oriel Instruments) equipped with a 400 nm long pass filter (to remove ultraviolet light) and a water filter (to remove infrared light) was used as the visible light source. At 30 minute intervals, 1 mL of the suspension was withdrawn using a syringe and filtered through a 0.2 μm PTFE syringe filter to remove the photocatalyst. The filtrate was diluted five times with deionized water and then Rhodamine B concentrations were determined using a UV-vis spectrometer (Perkin-Elmer Lambda 40) by measuring the peak intensity at 554 nm. For control studies, experiments were also conducted either in the dark, or without photocatalyst or without H_2O_2. The relative standard deviation for the photocatalytic tests was 4.3%.

3 Results and discussion

As illustrated in **Scheme 1**, CNNSs were synthesized through a two-step calcination-exfoliation method using urea as a precursor. The as-prepared CNNSs were then mixed with MIL-100(Fe) precursors for the *in situ* synthesis of CNNSs-MIL nanocomposites under mild conditions (95 ºC). Prior to evaluating the photocatalytic properties of the nanocomposites, the synthesized materials were first characterized in order to confirm their structure and chemistry. First, the crystalline structure of the parent materials as well as that of the nanocomposites was analysed. As seen in Figure 1, the inter-layer stacking peak intensity of CNNSs at 27.5º ((002) plane) was significantly reduced, indicating the exfoliation of CN. The MOF sample exhibited the expected pattern for MIL-100(Fe) although its crystallinity is lower than the simulated patterns due to the low- temperature synthesis at 95 ºC.[56] A similar pattern was observed for the CNNSs-MIL nanocomposites. This confirmed that a 5 wt% CNNSs loading did not prevent the formation of the MOF crystals. It is interesting to note that in

previous work on graphene oxide (GO)/MIL composites,[41] the crystallinity of the MIL component was affected in the presence of more than 4 wt% GO. This was attributed to a distortion of MIL caused by the interactions between the oxygen functional groups of GO and the metallic sites of MIL. Unlike GO, the main surface functional groups of CNNSs are uncondensed amino groups.[9] It is expected that these groups exhibit weaker interactions with the iron sites. Since CN is exfoliated, no peak representative of CNNSs was evident in the XRD patterns of the nanocomposites due to its weak intensity.

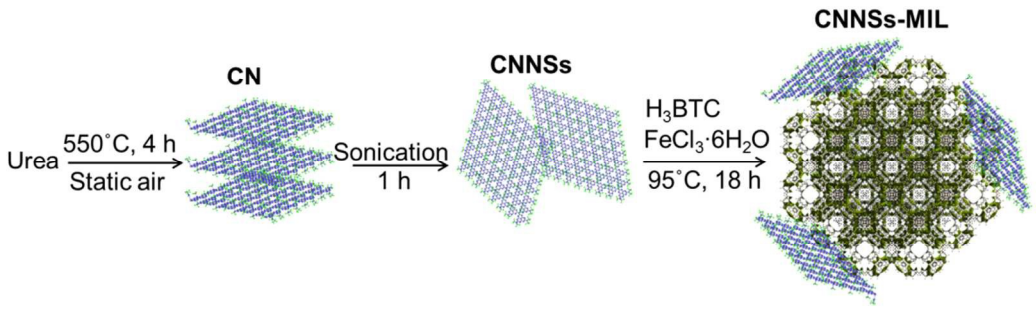

Scheme 1. Overview of the synthesis procedure of CNNSs-MIL nanocomposites. First step: synthesis of bulk CN via calcination of urea. Second step: exfoliation of bulk CN via sonication. Third step: synthesis of the MOF in the presence of dispersed CNNSs. Abbreviations: CN - bulk carbon nitride; CNNSs - carbon nitride nanosheets; H_3BTC - benzene-1,3,5-tricarboxylic acid; MIL - MIL-100(Fe).

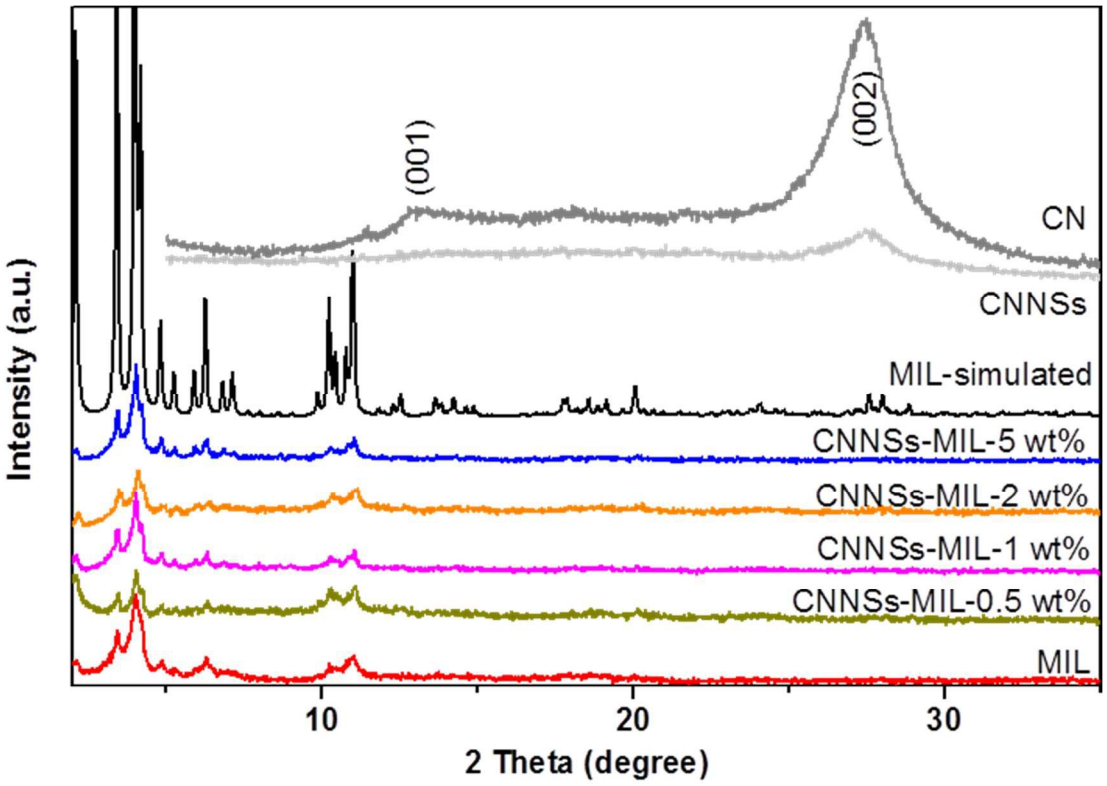

Figure 1. XRD patterns of bulk carbon nitride (CN), carbon nitride nanosheets (CNNSs), MIL-100(Fe), simulated MIL-100(Fe) (CCDC 640536) and the nanocomposites of CNNSs and MIL-100(Fe) with varying contents of CNNSs.

An important aspect of this study was to introduce porosity and enhance the surface area of the photocatalysts as a way to enable greater interactions between the reactants and the catalysts. Therefore, the porosity/surface area of the parent materials and nanocomposites were analysed using N_2 sorption. The N_2 isotherms of MIL, CNNSs, bulk CN and the various nanocomposites are shown in Figure S1. The textural parameters were calculated from the isotherms and the results are summarized in Table 1. The isotherms of bulk CN and CNNSs follow the type IV model, typical of mesoporous materials. Although no template was used to synthesise CN, irregular mesopores could be created via the release of the ammonia/carbon dioxide gas during the calcination of precursor urea. The specific surface area of CN and CNNSs were 70 $m^2 g^{-1}$ and 85 $m^2 g^{-1}$, respectively. The

surface area of CN was already high compared to that typically measured for CN synthesized using other precursors (e.g. melamine, cyanamide or dicyanamide) – usually around 10 $m^2 g^{-1}$.[57-59] Exfoliation led to a noticeable, albeit moderate, enhancement in porosity. This is due to the fact that CN synthesized from urea exhibits additional pores to those located between the layers. This is in contrast to CN synthesized from other precursors which typically exhibits a more condense structure with the porosity located purely in the interlayer space. Owing to the presence of pores in CN (from urea), the increase in surface area as a result of exfoliation was less pronounced. Typical type-I isotherms were observed for MIL as well as the nanocomposite samples. The surface area of MIL is found to be 1225 $m^2 g^{-1}$, which is in the reasonable range of reported surface area for MIL.[60] As seen in Table 1, increasing the CNNSs loading caused a decrease in the surface area and volume of pores of the composites compared to that of the parent MOF. Nevertheless, their surface area remained higher than 1000 $m^2 g^{-1}$. An indirect confirmation of the small decrease in porosity when building the nanocomposites was the minor decrease in adsorption capacity (for RhB) from 26.3% for MIL to 26.0% for CNNSs-MIL-1 wt%. The measured surface areas of the nanocomposites were compared to those of the corresponding physical mixtures. The latter were calculated taking into account the content of the parent materials in the composites and the surface area of the pure parent materials, e.g.:

$$S_{BET,CNNSs-MIL-1\,wt\%} = 0.01 \times S_{BET,CNNSs} + 0.99 \times S_{BET,MIL}$$

As shown in Table 1, the measured surface areas were slightly lower than the calculated ones. A potential explanation could be that a fraction of pores in the MOF were blocked by CNNSs. Another possibility is that the presence of the CNNSs in the mixture of precursors used to synthesise the MOFs, while not preventing, interfered with the formation of the MOF crystals. TEM was used to show the morphology/size of CN, CNNSs, MIL and CNNSs-MIL-1 wt% particles. The results are presented in Figure 2 and Figure S3. As seen from Figures 2A and 2B, the lateral size of CN particles largely decreased upon exfoliation. The MIL particles were clearly visible in the composite

(Figure 2D) but the presence of CNNSs was more difficult to detect. This is likely due to the very low CNNSs content in the composite.

Table 1. Textural parameters of bulk carbon nitride (CN), carbon nitride nanosheets (CNNSs), MIL-100(Fe) and the nanocomposites of CNNSs and MIL-100(Fe) with varying contents of CNNSs. These parameters were derived from the N_2 sorption isotherms obtained at -196 ^oC.

Samples	S_{BET} $m^2 g^{-1}$	$S_{BET\text{-}cal}$ [a] $m^2 g^{-1}$	V_{tot} $cm^3 g^{-1}$	V_{meso} $cm^3 g^{-1}$	V_{micro} [b] $cm^3 g^{-1}$
CNNSs	85	-	0.756	0.756	nil
CN	70	-	0.405	0.404	nil
MIL	1225	-	0.709	0.331	0.378
CNNSs-MIL-0.5 wt%	1122	1219	0.620	0.249	0.371
CNNSs-MIL-1 wt%	1096	1213	0.554	0.170	0.384
CNNSs-MIL-2 wt%	1013	1202	0.524	0.210	0.314
CNNSs-MIL-5 wt%	1006	1168	0.515	0.212	0.303

[a] Calculated BET surface area based on the hypothetical physical mixture of CNNSs and MIL. [b] Micropore volume was calculated from the t-plot method.

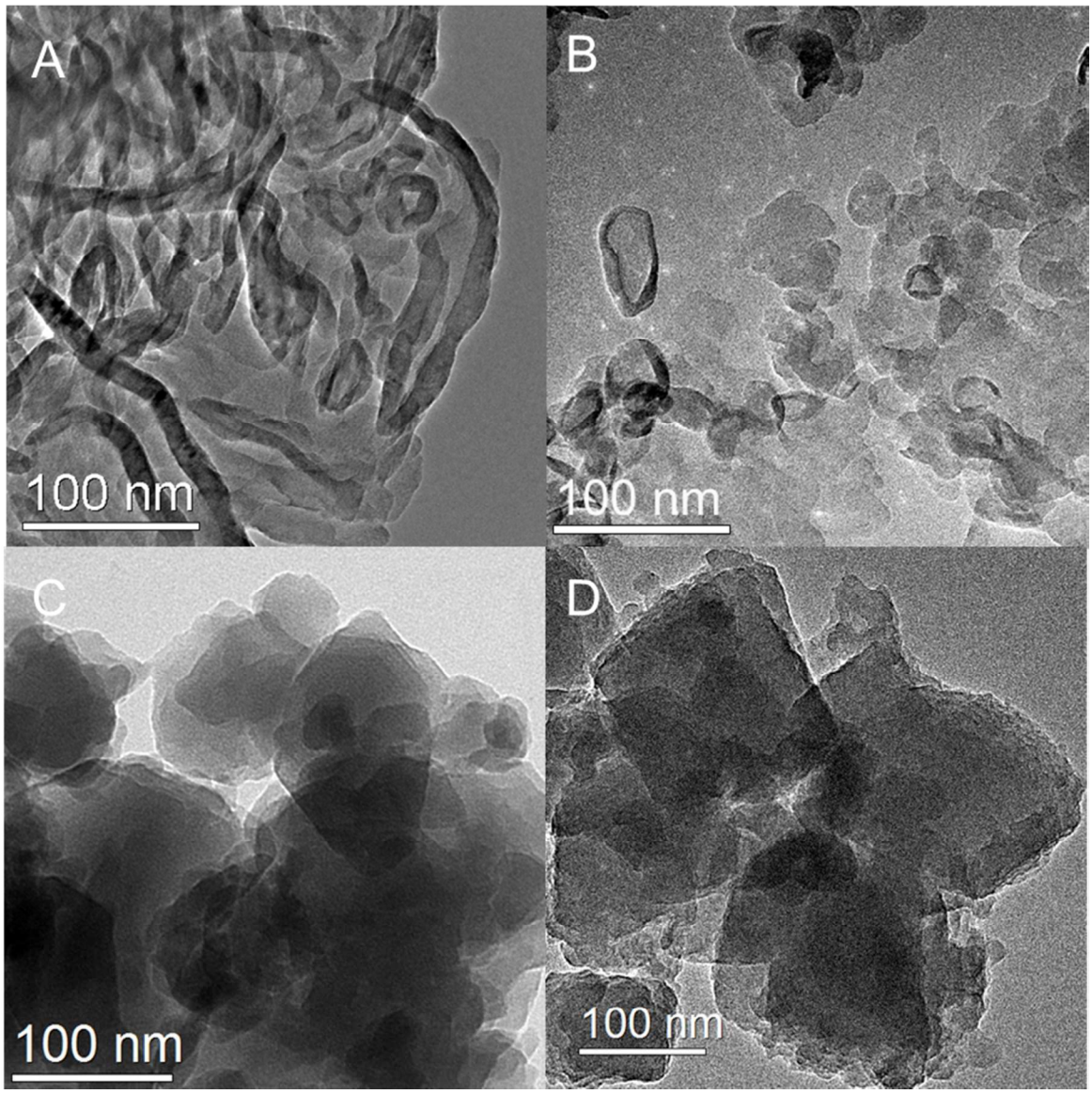

Figure 2. TEM images of: (A) carbon nitride (CN), (B) carbon nitride nanosheets (CNNSs), (C) MIL-100(Fe) and (D) CNNSs-MIL-1 wt% nanocomposite.

The presence of CNNSs in the nanocomposites was further confirmed using FT-IR spectroscopy (Figure 3). As expected, the same vibrational bands were observed for CN and CNNSs, indicating that while the structures of the two materials were different, the exfoliation did not introduce any major chemical changes. The presence of CNNSs in the nanocomposites was evident through the band at 800 cm^{-1}, which corresponds to the breathing mode of the triazine ring.[61]

However, this band was not visible in the spectrum of CNNSs-MIL-0.5 wt%, probably because of the low CNNSs content in that sample.

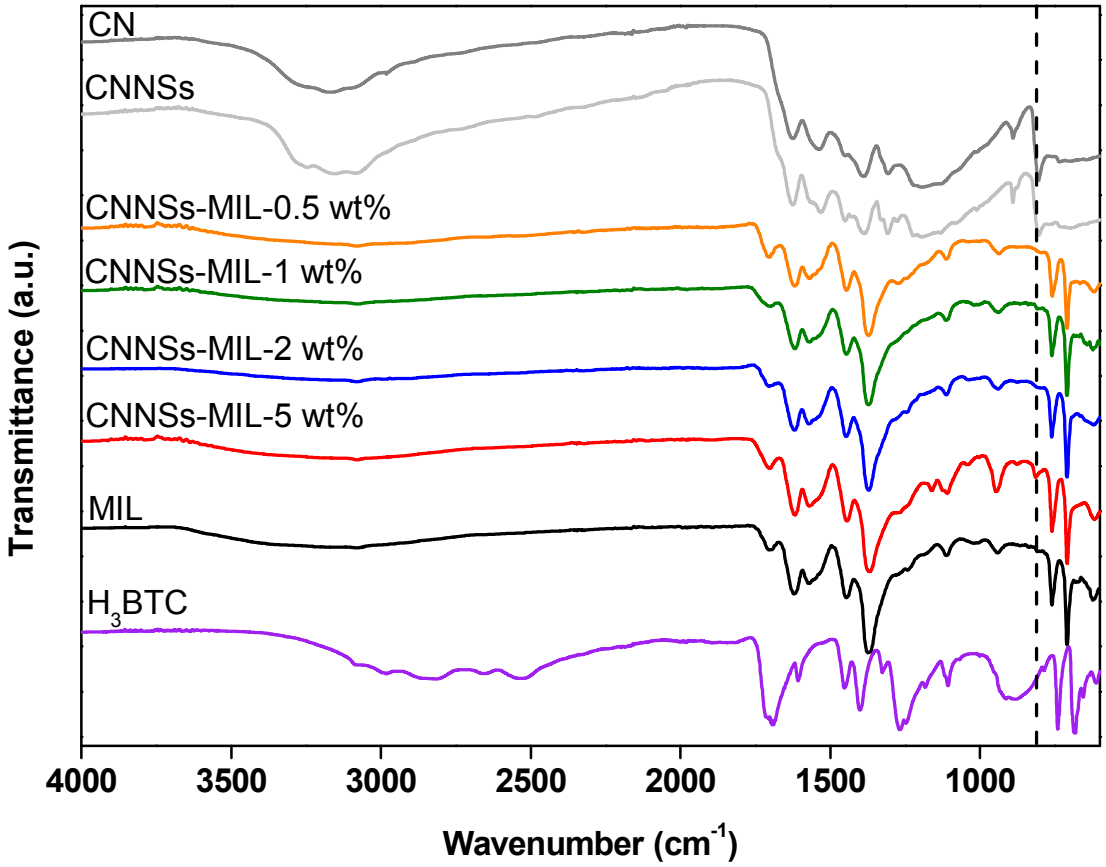

Figure 3. ATR FTIR spectra of bulk carbon nitride (CN), carbon nitride nanosheets (CNNSs), MIL-100(Fe) and the nanocomposites of CNNSs and MIL-100(Fe) with varying content of CNNSs.

Figure 4 shows the results of thermogravimetric analyses of CNNSs, MIL and their composites in air. CN was thermally stable up to 550 ºC, while the onset temperature was shifted to slightly lower temperatures for CNNSs. This was probably due to the introduction of defects/reduction of particle size caused by the exfoliation, which made CNNSs more prone to thermal combustion. Two-step weight loss were observed for MIL: (i) removal of water molecules bound to the iron trimmers weight loss (~10 wt%) from room temperature to 310 ºC and (ii) combustion of H_3BTC ligands of

the MOF (~60 wt%) between 310 ºC and 400 ºC.[51,56] Based on the molecular structure of MIL: $Fe_3O(H_2O)_2OH[C_6H_3(CO_2)_3]_2 \cdot nH_2O$, *n* was determined to be 4. The theoretical content of H_3BTC in MIL based on this molecular structure is 57.4 wt%, which is consistent with the experimental value from the thermogravimetric analysis (60.0 wt%). Thermogravimetric analysis was also carried out for the pure ligand (H_3BTC) and the mixture of $FeCl_3 \cdot 6H_2O$ with H_3BTC (H_3BTC wt% = 41%), the same weight ratio to that used for MIL synthesis. The weight loss between 310 ºC and 400 ºC for $FeCl_3 \cdot 6H_2O/H_3BTC$ mixture was 44 wt%, significantly lower than that of MIL (60 wt%). In addition, their TGA patterns are also different, indicating the chemical and composition changed from the precursors to MIL. As shown in Figure 4 and Figure S4, similar TGA patterns were found for the nanocomposites with different CNNSs contents. Interestingly, no mass decrease occurred for the nanocomposites at the temperature corresponding to the combustion of CNNSs. Although CNNSs are more stable than MIL, the presence of iron-containing MIL could potentially catalyse the decomposition of CNNSs under high temperature leading an 'earlier' decomposition. The decomposition of CN in the presence of metal ions (i.e. Ni^{2+}) via high temperature treatment has been reported previously.[10]

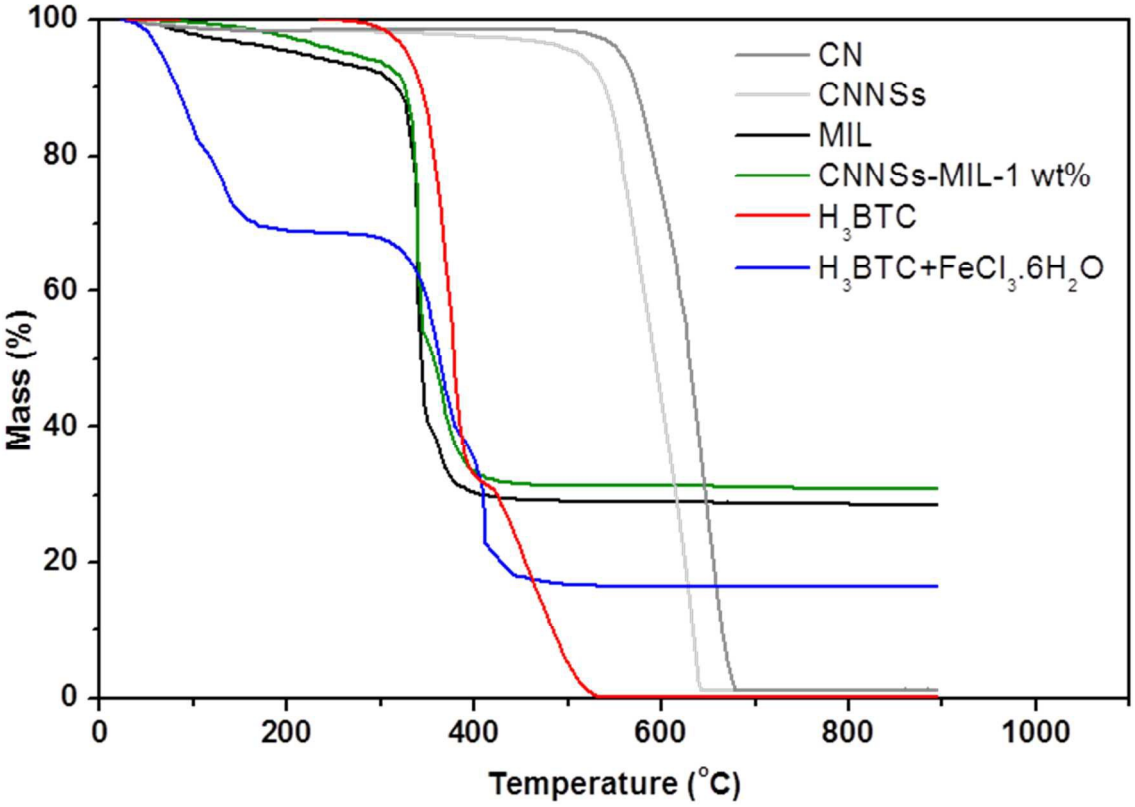

Figure 4. TGA curves of bulk carbon nitride (CN), carbon nitride nanosheets (CNNSs), MIL-100(Fe) and the nanocomposite CNNSs-MIL-1 wt%. Comparison is made with the physical mixture of $FeCl_3 \cdot 6H_2O$+H_3BTC (H_3BTC wt% = 41 %). The measurements were made in air.

PL spectroscopy was used as a way to probe the capacity of the nanocomposites to prevent electron-hole recombination. The PL emission spectra of MIL and CNNSs-MIL nanocomposites were recorded under excitation wavelengths of 395 nm. As seen in Figure 5A, CNNSs and MIL exhibited an emission peak at 440 nm, 554 nm, respectively. As CNNSs were added to form the nanocomposites, the emission peak remained at the same wavelength but its intensity decreased significantly (Figure 5B). These results demonstrated that rates of electron-hole recombination in the CNNSs-MIL nanocomposites decreased.[62] It is interesting to note that the physical mixture of CNNSs and MIL (1 wt%) also exhibited a decreased peak intensity, indicating that the physically mixed CNNSs interacted with MIL particles. However, the PL intensity reduction of the physical mixture was not as

pronounced as that observed for the nanocomposites. This must be due to the better dispersion achieved via in-situ synthesis compared to that obtained via physical mixing.

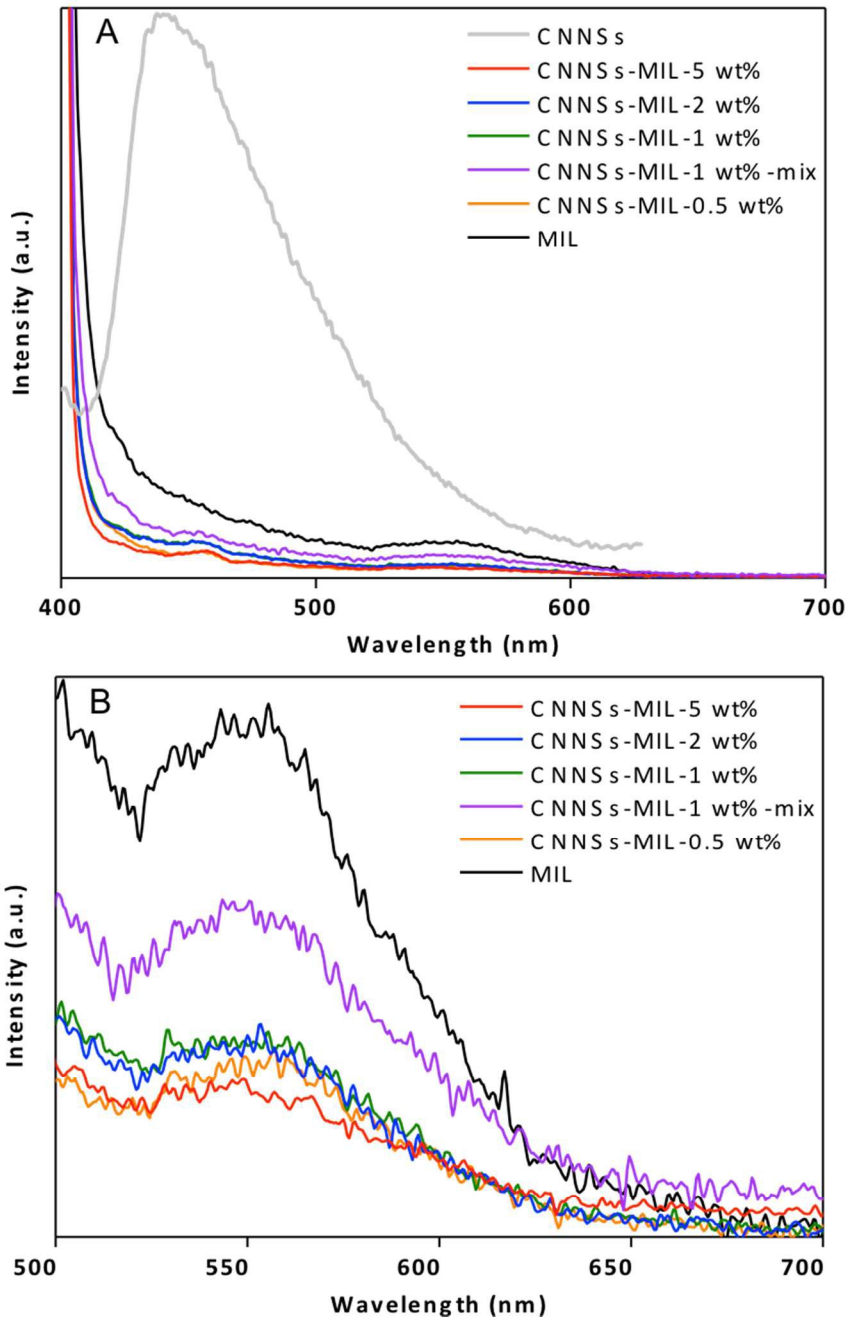

Figure 5. (A) PL spectra of MIL-100(Fe), the nanocomposites of CNNSs and MIL-100(Fe) with varying content of CNNSs, and physical mixture of CNNSs with MIL-100(Fe) (1 wt% of CNNSs); (B) Zoom-in of (A) without the spectrum of CNNSs (removed for greater clarity).

To understand how the formation of the nanocomposite could prevent electron-hole recombination, it was important to determine the electronic configuration of the materials and particularly their band gaps and band edge energies. For this, UV-vis DRS and electrochemical impedance spectroscopy (Mott-Schottky approach) were used, respectively. As seen in Figure 6, the absorption edge of CNNSs blue shifted by about 20 nm compared to bulk CN due to the quantum confinement effect.[45,46] Correspondingly, CNNSs became lighter in colour compared to bulk CN. MIL strongly absorbed visible light (400-600 nm), as evidenced by its dark brown sample colour. The nanocomposites exhibited a similar absorbance pattern to that of MIL. The CNNSs-MIL-1 wt% showed the strongest light absorbance, while a lower (0.5 wt%) or higher loading content (2 and 5 wt%) increased the light absorbance only slightly or even decreased the light absorbance, the trend of which was similar to that reported previously.[35] This change of light absorbance will affect the light harvesting capacity of the nanocomposites, thereby affecting their photocatalytic performance. From the UV-Vis DRS spectra, the band gaps of CNNSs and MIL were calculated to be 2.88 eV and 1.97 eV, respectively. The Mott- Schottky plots (Figure S5) were used to estimate the flat band potential and subsequently the conduction band.[9,34,43,63] It was found that capacitance values had a marginal frequency dependence. However, deviation from ideal behaviour was expected due to the nature and ways of material synthesis.[63] The conduction band (CB) of CNNSs and MIL were determined to be -0.92 V and -0.24 V, respectively, at pH 7. Based on these values, the band structures of CNNSs and MIL were determined and a schematic diagram is shown in Figure 7.

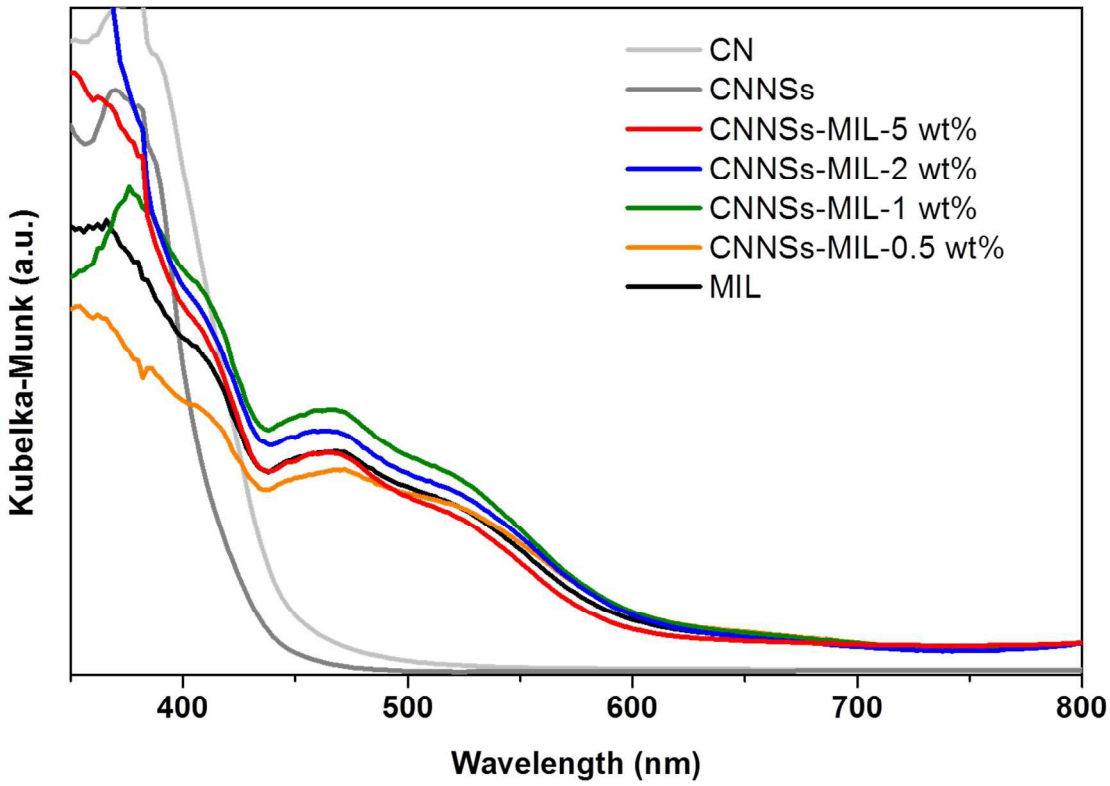

Figure 6. UV-vis DRS spectra of bulk carbon nitride (CN), carbon nitride nanosheets (CNNSs), MIL-100(Fe) and the nanocomposites of CNNSs and MIL-100(Fe) with varying contents of CNNSs.

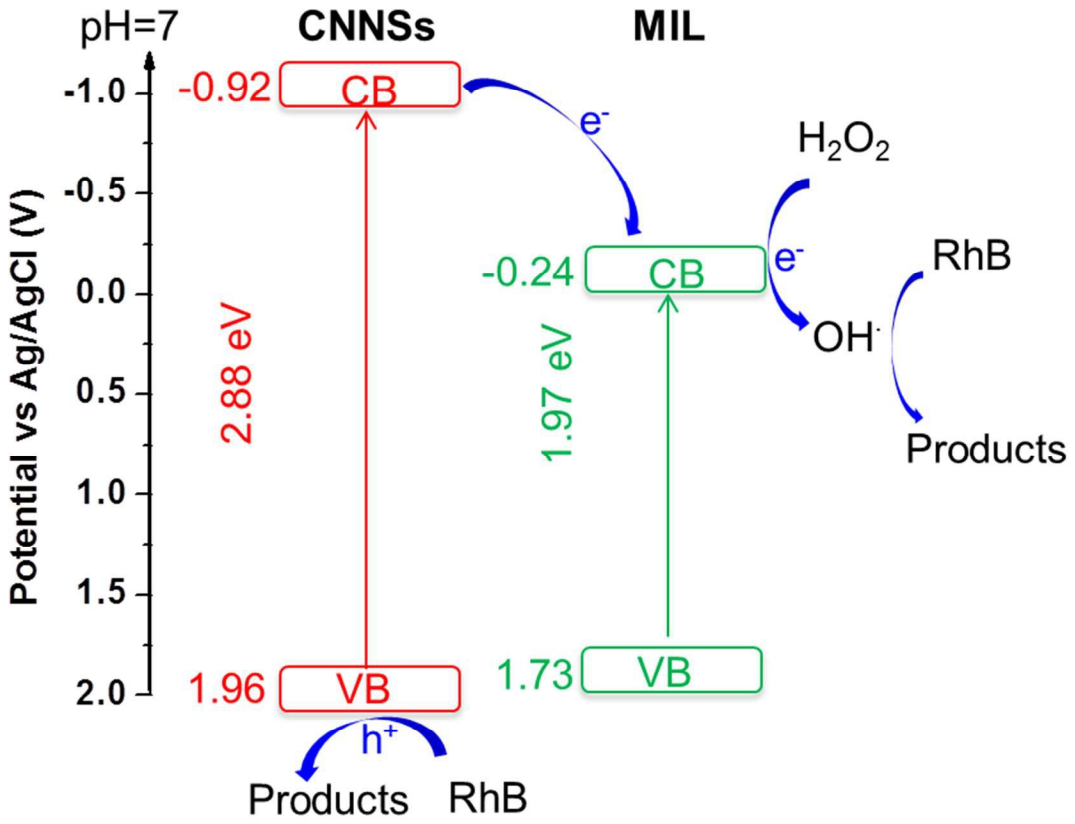

Figure 7. Band structure of the nanocomposites of CNNSs and MIL. Potential inhibition of electron-hole recombination is highlighted. A mechanism for the photocatalytic degradation of Rhodamine B using the nanocomposite is proposed. Abbreviations: CB - conduction band; VB - valence band.

As highlighted in Figure 7, a typical type-I straddling heterojunction between CNNSs and MIL could be formed in the nanocomposites.[40] The mechanism of organic molecules (e.g. Rhodamine B) degradation was proposed and is indicated on Figure 7. The various reactions involved in the process, along with their corresponding redox potentials, are described by Equations (1) to (13). Under visible light irradiation, electrons could be excited from the valence band (VB) of CNNSs to its conduction band (CB) and holes were simultaneously generated in the VB (Equation (1)). These electrons could then be easily transferred from the CB of CNNSs to that of MIL, the former being much more negative than the later, thereby separating electrons from holes in CNNSs. The accumulated electrons

in the CB of MIL could react with H_2O_2 and form hydroxyl radicals ($OH^{\cdot}$) (Equation (2)),[64] which are highly efficient for degradation of organics (Equation (6)).[65] The VB energy of CNNSs is very close to that of MIL, leading to less favourable hole transfer between their VBs.[66] Therefore, the holes in the VB of CNNSs were separated from electrons and could also be used for degradation of organics directly due to their strong oxidizing capability (Equation (7)).[34,67] It is however expected that the oxidation of organics using holes competes with the scavenging of holes by H_2O_2 (Equations (8), (10) and (12)).[64] Without forming nanocomposites, both MIL and CNNSs would be prone to electron-hole recombination. Besides, the light absorbance and surface area of CNNSs was much weaker/lower than that of MIL (Figure 6 and Table 1). In other words, the formation of the CNNSs-MIL nanocomposites allowed stronger light absorbance, higher surface area and more efficient electron-hole separation, which eventually led to a better photocatalytic performance.

$$Semiconductor + h\nu \underset{\text{recombination}}{\overset{\text{absorption}}{\rightleftharpoons}} Semiconductor(e_{CB}^{-}, h_{VB}^{+}) \quad (1)$$

$$H_2O_2 + H^+ + e^- \rightleftharpoons H_2O + OH^{\bullet} \quad (2)$$

$$@\ 298\ \text{K: } E_{H_2O_2/HO^{\bullet}}\ (\text{SHE})\ /\ \text{V} = 0.9881 - 0.0591pH + 0.0591\log\left(H_2O_2\right) - 0.0591\log\left(HO^{\bullet}\right) \quad (3)$$

$$OH^{\bullet} + H^+ + e^- \rightleftharpoons H_2O \quad (4)$$

$$@\ 298\ \text{K:} \quad E_{HO^{\bullet}/H_2O}\ (\text{SHE})\ /\ \text{V} = 2.5384 - 0.0591pH + 0.0591\log\left(HO^{\bullet}\right) \quad (5)$$

$$RhB + \nu_{OH^{\cdot}} OH^{\bullet} \longrightarrow \text{Products} \quad (6)$$

$$RhB + \nu_{h_{VB}^{+}} h_{VB}^{+} \longrightarrow \text{Products} \quad (7)$$

$$HO_2^{\bullet} + H^+ \rightleftharpoons H_2O_2 + h_{VB}^+ \quad (8)$$

@ 298 K: $E_{HO_2^{\bullet}/H_2O_2}$ (SHE) / V $= 1.4359 - 0.0591pH + 0.0591\log\left(HO_2^{\bullet}\right) - 0.0591\log\left(H_2O_2\right)$ (9)

$$O_2 + H^+ \rightleftharpoons HO_2^{\bullet} + h_{VB}^+ \quad (10)$$

@ 298 K: $E_{O_2/HO_2^{\bullet}}$ (SHE) / V $= -0.0460 - 0.0591pH - 0.0591\log\left(HO_2^{\bullet}\right) + 0.0591\log p_{O_2}$ (11)

$$O_2 + 2H^+ \rightleftharpoons H_2O_2 + 2h_{VB}^+ \quad (12)$$

@ 298 K: E_{O_2/H_2O_2} (SHE) / V $= 0.6949 - 0.0591pH + 0.0296\log p_{O_2} - 0.0296\log\left(H_2O_2\right)$ (13)

To evaluate the performance of the heterojunction structure formed, the nanocomposites were tested for the degradation of Rhodamine B (RhB). Their performances were compared to those of the parent materials, as well as that of the physical mixture of CNNSs and MIL. In addition, control studies were conducted without light or catalyst or hydrogen peroxide. The results are displayed in Figure 8A. The absence of light or catalyst resulted in no degradation, indicating the removal of RhB occurred by photocatalysis. Without H_2O_2, only 35% of RhB was degraded within 4 hours, while 100% degradation was reached after adding H_2O_2. As discussed above, two mechanisms of RhB degradation could be proposed: (i) direct reaction with holes in the VB of CNNSs and (ii) oxidation by $OH^{\cdot}$ radicals that formed from the reaction of electrons in MIL's CB with H_2O_2. The significant enhancement of RhB degradation after addition of H_2O_2 implied that the latter pathway was probably dominant.[67] The photocatalytic degradation results in Figure 8B show that separately CNNSs and MIL degraded respectively only 55% and 68% of RhB after 4 h of visible light irradiation. In comparison, CNNSs- MIL-0.5 wt% and CNNSs-MIL-1 wt% exhibited 77% and 100% removal, respectively. However, the performance decreased as the CNNSs loading was increased

beyond 1 wt%. This could be due to the presence of stacked CNNSs, which limited the homogeneous dispersion of the nanosheets, thereby leading to hole-electron recombination and decreasing light absorbance and surface area. Interestingly, the physical mixture containing 1 wt% of CNNSs performed better than the parent materials. However, the improvement was not as pronounced as that measured for the nanocomposites. This supports our hypothesis that the presence of a homogeneous well-mixed structure was the key.

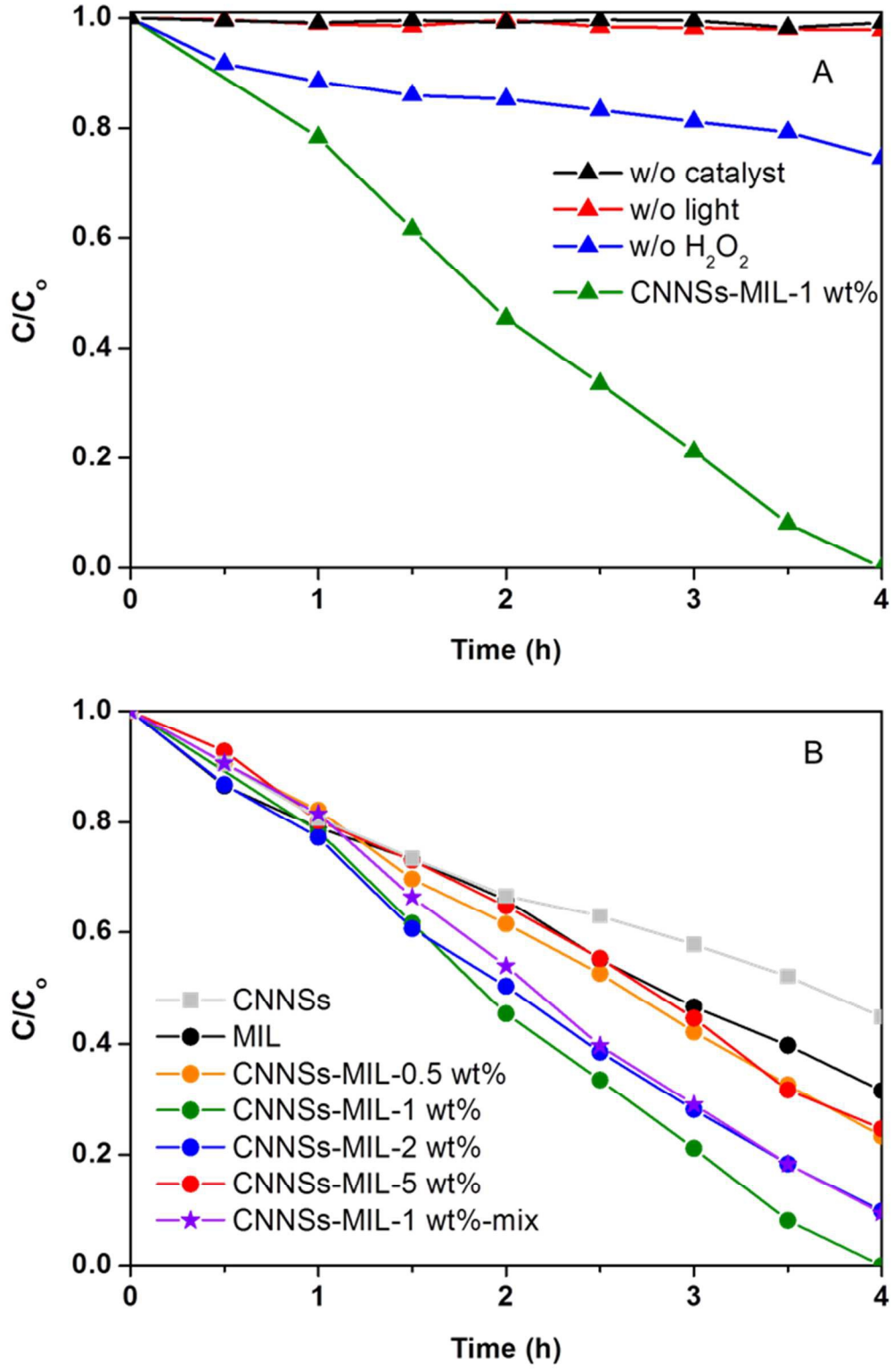

Figure 8. (A) Photocatalytic degradation of RhB under different control conditions. (B) Photocatalytic degradation of RhB over CNNSs, MIL, the nanocomposites of CNNSs and MIL-100(Fe) with varying contents of CNNSs, and the physical mixture of CNNSs and MIL (1 wt% of CNNSs). Conditions for

(A) and (B): 10 mg catalyst in 50 mL RhB aqueous solution (50 ppm), 0.01 M H_2O_2, Light source: 150 W Xe lamp equipped with 400 nm long pass filter.

To verify the stability of the nanocomposites upon light irradiation, CNNSs-MIL-1 wt% was characterized before and after photoreaction using XRD, FTIR and TGA. As shown in Figure 9A, the major XRD peaks remained, but their intensities decreased significantly, indicating that the structure of the composites was affected. No obvious change in the FTIR spectra (Figure 9B) was detected, indicating the functional groups were not affected by photo-irradiation. The TGA curve (Figure 9C) of the exhausted sample exhibited a larger weight loss below 310 ºC compared to the freshly synthesized composite. This could be due to the removal of adsorbed water and/or small organic molecules derived from RhB degradation, or possibly come from the decomposition of the organic ligand in the MOF, the structure of which may have been affected after the reaction (Figure 9A).

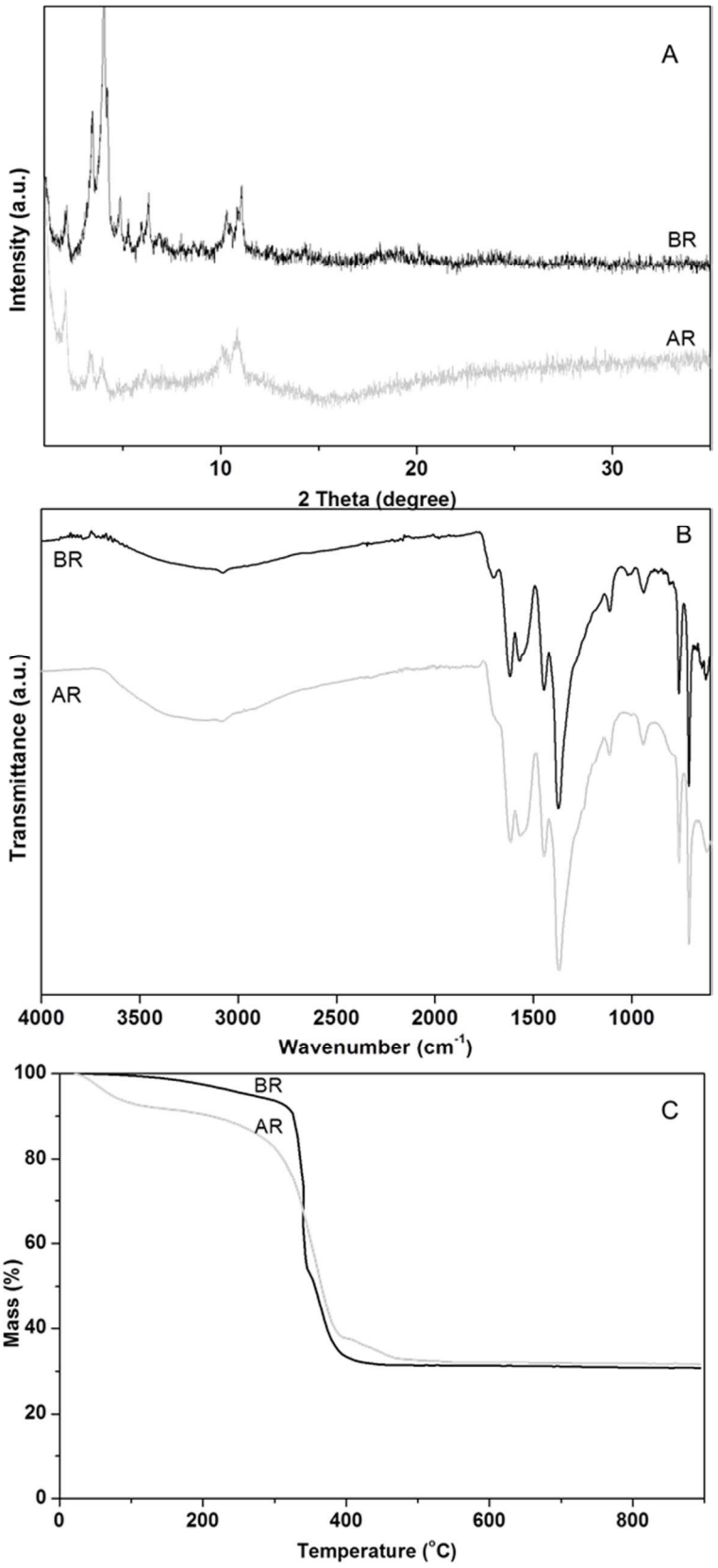

Figure 9. XRD patterns (A), FTIR spectrum, (B) and TGA curves (C) of CNNSs-MIL-1 wt% before (BR) and after (AR) photocatalytic reaction.

4 Conclusions

We have reported the *in situ* synthesis of carbon nitride nanosheets/metal-organic framework MIL-100(Fe) nanocomposites via a facile non-hydrothermal method. The CNNSs did not affect the MIL synthesis, while the strong light absorbance and high surface area of MIL were mainly retained in the nanocomposites. As a result, heterojunctions were formed in the nanocomposites exhibiting better electron-hole separation and therefore improved performance for dye degradation (up to 1.5 to 2 times higher) compared to the parent materials. The good dispersion of the CNNSs within the MOF matrix as well as the intimate contact between the nanosheets and the MOF particles governed the performance of the composites and enabled a significant improvement compared to the physical mixture. In addition, we found that the mechanism of hydroxyl radicals degradation outperformed the other mechanism of hole degradation. The findings here could serve as a basis for further development of photocatalysts involving MOF-based heterojunction and support the importance of the *in-situ* synthesis approach when preparing such composites.

Acknowledgements

This work was supported by the Department of Chemical Engineering at Imperial College. The authors are grateful to Dr. R. T. Woodward for assistance in materials preparation and P. Arcelus-Arrillaga for his help with the PL measurement.

References

1. A. Kudo and Y. Miseki, *Chem. Soc. Rev.*, 2009, **38**, 253-278.
2. S. C. Roy, O. K. Varghese, M. Paulose and C. A. Grimes, *ACS Nano*, 2010, **4**, 1259-1278.
3. M. R. Hoffmann, S. T. Martin, W. Choi and D. W. Bahnemann, *Chem. Rev.*, 1995, **95**, 69-96.
4. T. Zhang and W. B. Lin, *Chem. Soc. Rev.*, 2014, **43**, 5982-5993.

5. A. Fujishima and K. Honda, *Nature*, 1972, **238**, 37-38.
6. X. B. Chen, S. H. Shen, L. J. Guo and S. S. Mao, *Chem. Rev.*, 2010, **110**, 6503-6570.
7. X. C. Wang, K. Maeda, A. Thomas, K. Takanabe, G. Xin, J. M. Carlsson, K. Domen and M. Antonietti, *Nat. Mater.*, 2009, **8**, 76-80.
8. G. Liu, P. Niu, C. H. Sun, S. C. Smith, Z. G. Chen, G. Q. Lu and H.-M. Cheng, *J. Am. Chem. Soc.*, 2010, **132**, 11642-11648.
9. J. D. Hong, X. Y. Xia, Y. S. Wang and R. Xu, *J. Mater. Chem.*, 2012, **22**, 15006-15012.
10. J. D. Hong, Y. S. Wang, Y. B. Wang, W. Zhang and R. Xu, *ChemSusChem*, 2013, **6**, 2263-2268.
11. J. Mao, K. Li and T. Peng, *Catal. Sci. Tech.*, 2013, **3**, 2481-2498.
12. R. Kuriki, K. Sekizawa, O. Ishitani and K. Maeda, *Angew. Chem. Int. Ed.*, 2015, **54**, 2406-2409.
13. J. D. Hong, W. Zhang, Y. B. Wang, T. H. Zhou and R. Xu, *ChemCatChem*, 2014, **6**, 2315-2321.
14. Y. J. Cui, Z. X. Ding, P. Liu, M. Antonietti, X. Z. Fu and X. C. Wang, *Phys. Chem. Chem. Phys.*, 2012, **14**, 1455-1462.
15. J. D. Hong, S. M. Yin, Y. X. Pan, J. Y. Han, T. H. Zhou and R. Xu, *Nanoscale*, 2014, **6**, 14984-14990.
16. J.-R. Li, R. J. Kuppler and H.-C. Zhou, *Chem. Soc. Rev.*, 2009, **38**, 1477-1504.
17. J. Y. Lee, O. K. Farha, J. Roberts, K. A. Scheidt, S. T. Nguyen and J. T. Hupp, *Chem. Soc. Rev.*, 2009, **38**, 1450-1459.
18. A. Corma, H. Garcia and F. Llabrés i Xamena, *Chem. Rev.*, 2010, **110**, 4606-4655.
19. L. E. Kreno, K. Leong, O. K. Farha, M. Allendorf, R. P. Van Duyne and J. T. Hupp, *Chem. Rev.*, 2011, **112**, 1105-1125.
20. P. Horcajada, T. Chalati, C. Serre, B. Gillet, C. Sebrie, T. Baati, J. F. Eubank, D. Heurtaux, P. Clayette and C. Kreuz, *Nat. Mater.*, 2010, **9**, 172-178.
21. S. B. Wang and X. C. Wang, *Small*, 2015, **11**, 3097–3112.
22. F. X. L. i. Xamena, A. Corma and H. Garcia, *J. Phys. Chem. C*, 2007, **111**, 80-85.
23. T. H. Zhou, Y. D. Du, A. Borgna, J. D. Hong, Y. B. Wang, J. Y. Han, W. Zhang and R. Xu, *Energy Environ. Sci.*, 2013, **6**, 3229-3234.

24. D. R. Sun, Y. H. Fu, W. J. Liu, L. Ye, D. K. Wang, L. Yang, X. Z. Fu and Z. H. Li, *Chem.-Eur. J.*, 2013, **19**, 14279-14285.
25. J.-J. Zhou, R. Wang, X.-L. Liu, F.-M. Peng, C.-H. Li, F. Teng and Y.-P. Yuan, *Appl. Surf. Sci.*, 2015, **346**, 278-283.
26. R. Wang, L. N. Gu, J. J. Zhou, X. L. Liu, F. Teng, C. H. Li, Y. H. Shen and Y. P. Yuan, *Adv. Mater. Interfaces*, 2015, Doi: 10.1002/admi.201500037.
27. C. Wang, Z. Xie, K. E. deKrafft and W. Lin, *J. Am. Chem. Soc.*, 2011, **133**, 13445-13454.
28. J. K. Gao, J. W. Miao, P.-Z. Li, W. Y. Teng, L. Yang, Y. L. Zhao, B. Liu and Q. C. Zhang, *Chem. Commun.*, 2014, **50**, 3786-3788.
29. J.-J. Du, Y.-P. Yuan, J.-X. Sun, F.-M. Peng, X. Jiang, L.-G. Qiu, A.-J. Xie, Y.-H. Shen and J.-F. Zhu, *J. Harzard Mater.*, 2011, **190**, 945-951.
30. D. K. Wang, R. K. Huang, W. J. Liu, D. R. Sun and Z. H. Li, *ACS Catal.*, 2014, **4**, 4254-4260.
31. W.-T. Xu, L. Ma, F. Ke, F.-M. Peng, G.-S. Xu, Y.-H. Shen, J.-F. Zhu, L.-G. Qiu and Y.-P. Yuan, *Dalton Trans.*, 2014, **43**, 3792-3798.
32. K. G. Laurier, F. Vermoortele, R. Ameloot, D. E. De Vos, J. Hofkens and M. B. Roeffaers, *J. Am. Chem. Soc.*, 2013, **135**, 14488-14491.
33. C.-F. Zhang, L.-G. Qiu, F. Ke, Y.-J. Zhu, Y.-P. Yuan, G.-S. Xu and X. Jiang, *J. Mater. Chem. A*, 2013, **1**, 14329-14334.
34. F. Ke, L. H. Wang and J. F. Zhu, *Nano Res.*, 2015, **8**, 1834-1846.
35. Y. L. Xu, M. M. Lv, H. B. Yang, Q. Chen, X. T. Liu and F. Y. Wei, *RSC Adv.*, 2015, **5**, 43473-43479.
36. Y. Fu, D. Sun, Y. Chen, R. Huang, Z. Ding, X. Fu and Z. Li, *Angew. Chem. Int. Ed.*, 2012, **51**, 3364-3367.
37. H. Wang, X. Z. Yuan, Y. Wu, G. M. Zeng, X. H. Chen, L. J. Leng and H. Li, *Appl. Catal. B Environ.*, 2015, **174**, 445-454.
38. H. L. Wang, L. S. Zhang, Z. G. Chen, J. Q. Hu, S. J. Li, Z. H. Wang, J. S. Liu and X. C. Wang, *Chem. Soc. Rev.*, 2014, **43**, 5234-5244.
39. Y.-P. Yuan, L.-W. Ruan, J. Barber, S. C. J. Loo and C. Xue, *Energy Environ. Sci.*, 2014, **7**, 3934-3951.
40. H. J. Li, Y. Zhou, W. G. Tu, J. H. Ye and Z. G. Zou, *Adv. Funct. Mater.*, 2015, **25**, 998-1013.

41. C. Petit and T. J. Bandosz, *Adv. Funct. Mater.*, 2011, **21**, 2108-2117.

42. N. C. Burtch, H. Jasuja and K. S. Walton, *Chem. Rev.*, 2014, **114**, 10575-10612.

43. R. W. Liang, F. F. Jing, L. J. Shen, N. Qin and L. Wu, *Nano Res.*, 2015, **8**, 3237-3249.

44. S. B. Wang, J. L. Lin and X. C. Wang, *Phys. Chem. Chem. Phys.*, 2014, **16**, 14656-14660.

45. P. Niu, L. L. Zhang, G. Liu and H. M. Cheng, *Adv. Funct. Mater.*, 2012, **22**, 4763-4770.

46. X. D. Zhang, X. Xie, H. Wang, J. J. Zhang, B. C. Pan and Y. Xie, *J. Am. Chem. Soc.*, 2013, **135**, 18-21.

47. C. Petit and T. J. Bandosz, *Adv. Mat.*, 2009, **21**, 4753-4757.

48. C. Petit and T. J. Bandosz, *J. Mater. Chem.*, 2009, **19**, 6521-6528.

49. C. Petit and T. J. Bandosz, *Adv. Funct. Mater.*, 2010, **20**, 111-118.

50. C. Petit, B. Levasseur, B. Mendoza and T. J. Bandosz, *Micropor. Mesopor. Mater.*, 2012, **154**, 107-112.

51. F. M. Zhang, J. Shi, Y. Jin, Y. H. Fu, Y. J. Zhong and W. D. Zhu, *Chem. Eng. J.*, 2015, **259**, 183-190.

52. S. Brunauer, P. H. Emmett and E. Teller, *J. Am. Chem. Soc.*, 1938, **60**, 309-319.

53. B. Lippens and J. De Boer, *J. Catal.*, 1965, **4**, 319-323.

54. I. Horcas, R. Fernández, J. Gomez-Rodriguez, J. Colchero, J. Gómez-Herrero and A. Baro, *Rev. Sci. Instrum.*, 2007, **78**, 013705.

55. G. Kortüm, W. Braun and G. Herzog, *Angew. Chem. Int. Ed.*, 1963, **2**, 333-341.

56. P. Horcajada, S. Surblé, C. Serre, D.-Y. Hong, Y.-K. Seo, J.-S. Chang, J.-M. Greneche, I. Margiolaki and G. Férey, *Chem. Commun.*, 2007, 2820-2822.

57. X. C. Wang, K. Maeda, X. F. Chen, K. Takanabe, K. Domen, Y. D. Hou, X. Z. Fu and M. Antonietti, *J. Am. Chem. Soc.*, 2009, **131**, 1680-1681.

58. J. Xu, Y. J. Wang and Y. F. Zhu, *Langmuir*, 2013, **29**, 10566-10572.

59. Y. Huang, Y. J. Wang, Y. Q. Bi, J. R. Jin, M. F. Ehsan, M. Fu and T. He, *RSC Adv.*, 2015, **5**, 33254-33261.

60. Y.-K. Seo, J. W. Yoon, J. S. Lee, U.-H. Lee, Y. K. Hwang, C.-H. Jun, P. Horcajada, C. Serre and J.-S. Chang, *Micropor. Mesopor. Mater.*, 2012, **157**, 137-145.

61. J. S. Zhang, X. F. Chen, K. Takanabe, K. Maeda, K. Domen, J. D. Epping, X. Z. Fu, M. Antonietti and X. C. Wang, *Angew. Chem. Int. Ed.*, 2010, **49**, 441-444.

62. K. Maeda, K. Teramura and K. Domen, *J. Catal.*, 2008, **254**, 198-204.

63. R. Beranek, *Adv. Phys. Chem.*, 2011, ID 786759.

64. P. Pichat, C. Guillard, L. Amalric, A.-C. Renard and O. Plaidy, *Sol. Energy Mater. Sol. Cells*, 1995, **38**, 391-399.

65. C. S. Turchi and D. F. Ollis, *J. Catal.*, 1990, **122**, 178-192.

66. J. Su, X.-X. Zou, G.-D. Li, X. Wei, C. Yan, Y.-N. Wang, J. Zhao, L.-J. Zhou and J.-S. Chen, *J. Phys. Chem. C*, 2011, **115**, 8064-8071.

67. N. Daneshvar, D. Salari and A. Khataee, *J. Photochem. Photobiol. A*, 2004, **162**, 317-322.

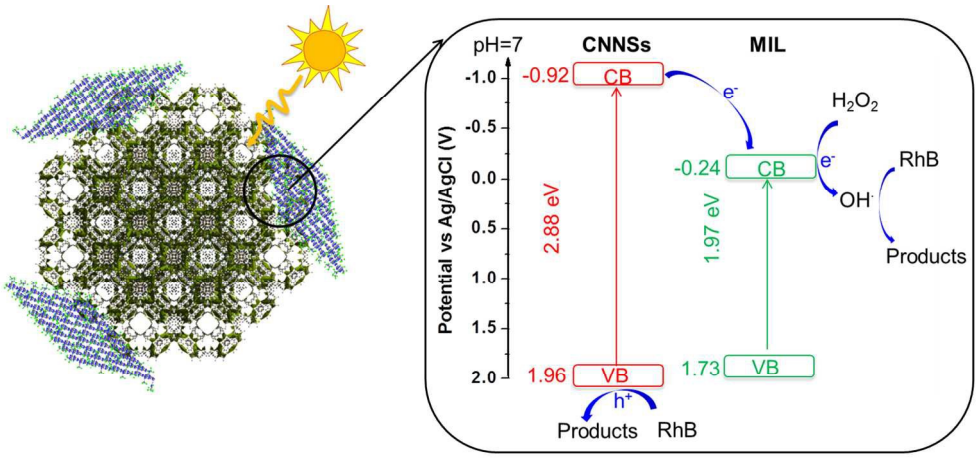

268x123mm (150 x 150 DPI)